Computations of Multiphase Flows by a Finite Difference/Front Tracking Method. III. Variable Surface Tension and Phase Change

G. Tryggvason,
D. Juric, J. Che, M.R.H. Nobari, and S. Nas

Abstract

In part I of these notes, a numerical method to simulate the motion of two fluids is presented. The basic approach is to write one set of governing equations for all of the fluids involved and account for interfacial terms by adding the appropriate sources as delta functions at the interface. The governing equations are solved on a fixed grid, and the interface is explicitly tracked by a moving grid, or front, of a lower dimension than the fixed grid. Several extensions of this numerical method to flows with more complex physics are described here.

Two sets of simulations with variable surface tension are described. The effect of an immiscible surfactant on the rise of axisymmetric bubbles is examined, and it is shown that the surfactant immobilizes the interface and usually reduces the rise velocity of the bubbles. For deformable bubbles, the presence of a surfactant reduces the deformation. In some cases, the reduction in deformation decreases the pressure drag more than it increases the viscous drag; therefore, the contaminated bubble rises faster than a clean one. Simulations of bubbles and drops in flows with a temperature gradient show that the bubbles move toward the hotter side if the surface tension coefficient decreases with temperature. In some cases, the bubbles show a strong tendency to line up perpendicular to the temperature gradient.

Several extensions to flow with phase change are also described. The simplest solidification model is to assume that a fluid solidifies if the temperature drops below the solidification temperature. This model has been used to study the solidification of drops impacting a cold wall. More complex phase change models account for the release of latent heat at the phase boundary, as well as curvature effects on the interface temperature. A method for the phase change of both pure materials and binary alloys in the absence of flow is described and examples of the unstable growth of both dendritic and cellular solidification front is shown. The method is then extended to include fluid flow and applied to film boiling. This requires the solution of the Navier-Stokes and energy equations with interphase mass transfer. The growth and dynamics of a vapor layer adjacent to an upward facing, flat, heated surface has been studied. Vaporization of the liquid at the liquid-vapor interface continually replenishes the vapor lost due to bubble departure from the interface.

1 Introduction

In most applications, fluid flow is only part of the process and additional physical phenomena must be included for a complete picture. Most often the combination of phase change with fluid flow and heat transfer determines the efficacy of heat transfer equipment or the microstructure of solidified alloys. For instance, electrical properties of semiconductors and mechanical properties of single crystal turbine blades are closely coupled to fluid convection and processing conditions during directional solidification. Research on advanced materials and manufacturing processes such as rapid solidification or spray casting for the production of net or near-net shape components depends on the ability to understand and control fluid flow during solidification. The power generation industry takes advantage of the high heat transfer rates associated with phase change in boiling to extract energy from solar, fossil, and nuclear fuels.

Experimental investigations of phase change in solidification and boiling are typically difficult due to the large range of important time and length scales involved. Numerical simulations are a promising complement to experimental investigations and provide information that is hard to measure. For example, the harsh thermal and chemical environments and limited optical access in directional solidification furnaces often make it impossible to obtain detailed measurements.

Computations of flows with phase change are still far behind what is possible for multifluid flows. Indeed most computations that attempt to model any complexity in the physic are limited to very simple geometry. For example, the simulations of melting by Liu *et al.* (1993) and Schunk and Rao (1994) who used a two-dimensional finite element method to model the drying and cooling of a dip coating process. Although the physics is fairly complex, the geometry is not. For simple solidification of a pure material, with no flow, several authors have computed complex interface shapes using several methods. Those include boundary integral methods (Brattkus and Meiron, 1992), and the so called phase field models (Kobayashi, 1992; Wheeler, Murray, and Schaefer, 1993; Braun, McFadden, and Coriell, 1994). Simulations of complex three-dimensional dendritic growth are still very rare (Schmidt, 1996). Flows in which unsteady solidification is combined with unsteady fluid flow are most successfully modeled using the enthalpy method. However, this method is not well suited for a detailed description of interfacial physics. Consequently, it has been used mostly for computations aimed at capturing the large scale evolution where small scale effects are modeled by a "mushy zone." Examples of such computations can be found in Swaminathan and Voller (1993) and Shyy and Rao (1994).

Here, we discuss several extensions of the methodology presented in note I to more complex physical problems. First, we show results for flows with variable surface tension due to surfactant and variable temperature effects. Phase change is then discussed. We begin with a simple solidification model, in which the liquid is immobilized when the temperature drops below a prescribed value, to examine the shape of drops impacting a cold wall. More complex phase change models account for the release of latent heat at the phase boundary, as well as the effect of curvature on the interface temperature. A method for the phase change of both pure materials and binary alloys in the absence of flow is described. This method is then extended to include fluid flow and applied to film

boiling.

2 Variable Surface Tension

2.1 Contaminated Bubbles

The analytical solution for a bubble or a drop moving at low Reynolds numbers, was obtained independently by Hadamard (1911) and Rybczynski (1911). It was discovered very early that small bubbles or droplets do not obey this law, instead they behave more like a solid sphere. Theoretical analysis of a moving solid sphere gives terminal velocity a fifty percent lower than for a fluid sphere, which is in agreement with the results of Bond (1927) and Bond and Newton (1928) for small bubbles. Experimental investigations have since shown that it is actually the impurities in the fluids, usually called "surface-active agents", "surfactants" or "contaminants", that influence bubble behavior. For instance, Harberman and Morton (1956) reported that bubbles behave differently in distilled water and tap water. In the latter case, the terminal velocity is reduced, and the drag coefficient is increased.

The observed effect of contamination results directly from the retardation of the interfacial velocity which is well explained by the surface tension gradient model proposed by Frumkin and Levich (1947). Because surface tension depends on the concentration of surface-active materials, or contaminants, uneven distribution of these materials will lead to surface forces. Surface tension is generally reduced by an increase in concentration of contaminants, which induces forces that redistribute the contaminant more uniformly. As a bubble moves through a fluid, contaminant is swept from the front of the bubble to the back generating a force that immobilizes the surface.

To analyze the flow pattern around a contaminated bubble, extra equations are required for the transport of the contaminant, in addition to the usual conservation equations for mass and momentum. These equations are coupled with the Navier-Stokes equations through an equation of state, which relates the surface tension coefficient to the local concentration of the contaminant. All equations must be solved simultaneously. Although many theoretical studies of this problem have been reported, they are generally rather limited in scope and either have to assume a surface tension gradient profile, to avoid solving the additional equation, or have to use greatly simplified equations for the transport of the contaminant. Nevertheless, analyses based on these simplifications have given good descriptions of the dynamics of contaminated bubbles moving at low Reynolds numbers. To date, the effect of contamination on bubble deformation at large Reynolds numbers is not well understood and no numerical studies have been reported. For a review of the behavior of both clean and contaminated bubbles, see the articles by Harper (1972,1973).

Computations of the rise of contaminated bubbles at both low and high Reynolds number are presented. These simulations assume an insoluble contaminant, negligible bulk diffusion, and use a linear equation of state to relate surface tension to the surfactant concentration. The strength of the surfactant can then be represented by a single parameter, thus keeping track of the surfactant concentration is straight forward, because

it is simply inversely proportional to the stretching of the element.

The results of four calculations are shown in Figure 1, where the nondimensional strength of the contaminant, $E = (\gamma_o/\sigma_o)(d\sigma/d\gamma)$, is varied but the Eötvös number and the Morton number are held constant. Here, γ is the concentration of contaminant and σ is the surface tension. The Eötvös number and the Morton number are defined by: $Eo = \rho_o g d_e/\sigma$ and $M = g\mu^4/\rho\sigma^3$ where ρ is the density, μ is the viscosity, and d_e is the diameter of the initially spherical bubble. The initial conditions are shown at the bottom of each column and each bubble and the contaminant distribution is shown at three equal time intervals as the bubbles rise. Initially each bubble is spherical, and the contaminant is distributed uniformly over the bubble surface. The contaminant concentration is plotted as dashed lines perpendicular to the bubble interface (thick, solid line), with the length of the dashed lines proportional to the concentration (the actual thickness of the contaminant layer is only a few molecular diameters). Here, $Eo = 10$, $M = 10^{-3}$, and the density ratio and the viscosity ratio are both equal to 40. The numerical resolution is generally about twenty five mesh points per bubble radius, or 129 by 512 points for the whole computational domain. Extensive convergence studies suggest that for the range of parameters studied here, the solution is essentially fully converged at this resolution. For problems where the range of scales is larger, i.e., at higher Reynolds numbers, a finer resolution would be necessary; conversely, for lower Reynolds number a lower resolution would be sufficient.

Qualitatively, the effect of contamination on the bubbles is obvious by examination of Figure 1. In each case, the initially spherical bubble is deformed into an elliptical shape as it rises, and after an initial transient, the bubbles rise with a constant velocity and shape. The bubble in the column on the left has a completely passive contaminant, $E = 0$, where the surface tension does not depend on the contaminant concentration and no shear force is produced as a result of the redistribution of the contaminant. So, it is identical to a clean bubble with a surface tension coefficient equal to $\sigma(c_o)$. For contaminated bubbles, such as the bubble in column two, where $E = -1.6$, a redistribution of the contaminant results in a surface tension gradient. As the clean bubble rises, the contaminant is continuously swept from the front of the bubble to the back. For contaminated bubbles, initially the oncoming flow sweeps the contaminant to the back increasing the surface tension at the front, and decreasing it at the back. This induces a tangential interfacial force that opposes the flow. Finally, a steady-state distribution of the contaminant concentration is achieved as a result of the balance of the viscous shear from the oncoming flow and the tangential force due to the surface tension gradient. As a consequence, the rise velocity of the bubble is reduced considerably, since the bubble interface is no longer fully mobile, but has become nearly a no-slip one. The resulting deformation of the bubble is also smaller. Notice that the concentration of the contaminant is nearly constant at the back of the bubble, but increases gradually over the front. When the strength of the contaminant is increased, such as for the bubbles in columns three ($E = -3.2$) and four ($E = -6.4$), the bubbles behave much like the bubble in column two. Compared to the clean bubble, the contaminant variations are much smaller and the bubbles rise much slower. Although there is a noticeable difference in the contaminant distribution between the three bubbles on the right, they all have the same terminal velocity. In addition, the shape of the

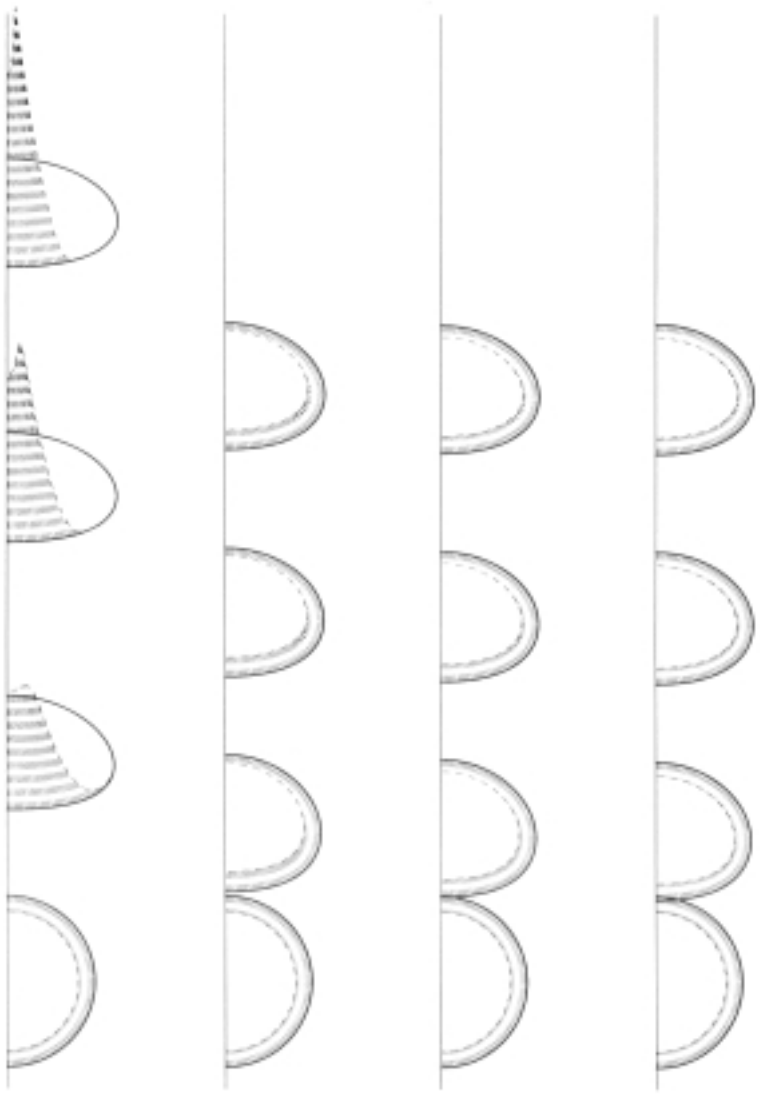

Figure 1: The rise of bubbles covered by an insoluble surfactant. The bubbles and the concentration of the surfactant are shown at four times for four simulations with increasing surfactant strength from left to right.

contaminated bubbles, which are more spherical, differ considerably from the clean one, but relatively little from each other.

Several other computations examine the rise of contaminated bubbles in a gravity field in some detail. The results are in agreement with experimental observations and show that contamination generally slows the bubbles down, and that once sufficiently contaminated, no further changes take place. More specifically we have shown:

- The contaminant is redistributed on the bubble surface until the shear due to the surface tension gradient is balanced by the oncoming flow. The bubble surface is then immobile with respect to the bubble.

- An immobile bubble surface generally leads to a larger wake; therefore, the form drag increases in addition to an increase in viscous drag.

- Early separation for bubbles with an immobile surface generally results in less curvature of the streamlines, thus less pressure drop at the bubble edge resulting in less deformation. For high Morton and Eötvös numbers, this reduction in bubble deformation can be so large that the resulting wake is actually smaller than for a clean bubble producing less drag. Thus, we find that for deformed bubbles the increased drag due to the immobilization of the interface can be offset by reduced deformation.

2.2 Thermocapillary Motion of Drops

Bubbles and drops in an ambient fluid with a temperature gradient will move toward the hot region due to thermocapillary forces. Surface tension usually decreases with increasing temperature. This nonuniform surface tension at the bubble surface causes shear stresses that are transmitted to the outer fluid by viscous forces inducing a motion of the bubble in the direction of the thermal gradient. In space, where buoyancy forces are negligible, thermocapillary forces can be dominant. For material processing in microgravity, thermal migration can be used to remove gas bubbles or liquid drops in melts before solidification. Thermocapillary migration can also be important in the design of two-phase heat exchangers for space applications. Accumulation of bubbles on heated surfaces can act as an insulator and prevent heat transfer to the surface.

While considerable effort has been devoted to understanding the thermocapillary migration of a single particle, bubble or drop, only a few researchers have looked at the collective behavior of two or more particles. Practical applications deal with many particles and their collective behavior may differ substantially from that of a single particle. The motion of two bubbles in a flow where the motion is governed by the Stokes equations and the temperature can be assumed to be quasi-steady has been examined by several investigators. This work was generalized to an arbitrary number of equal size bubbles by Acrivos, Jeffrey, and Saville (1990) who showed that each bubble moves independently of the other bubbles. This remarkable result is, however, restricted to very slow motion in a highly conducting fluid (zero Reynolds and Marangoni numbers). Here, we examine the motion of several equal size bubbles when these numbers are non-zero.

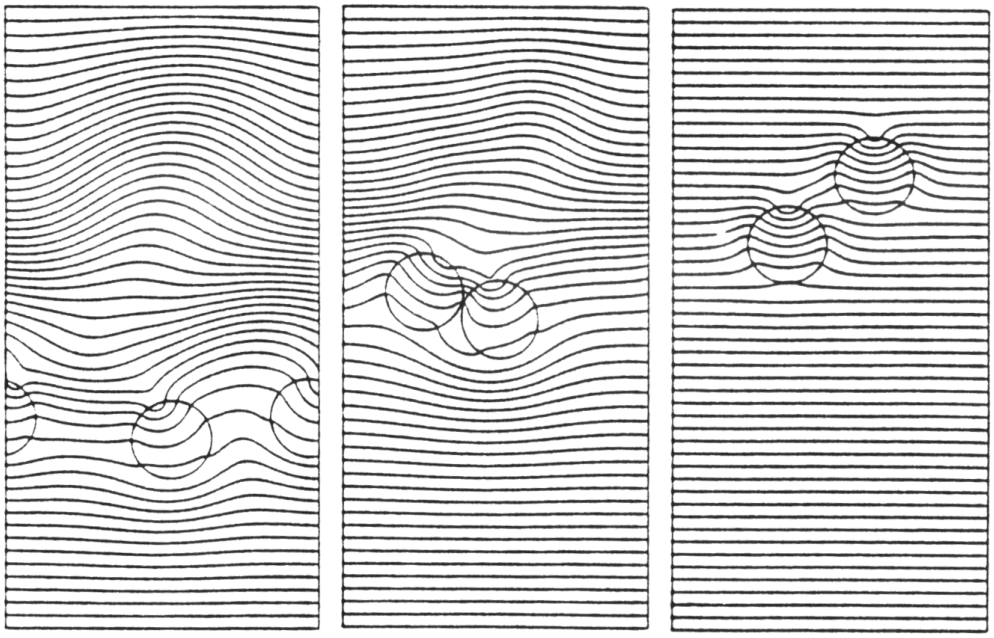

Figure 2: Thermocapillary migration of two two-dimensional bubbles. The bubbles and the isotherms are shown at three times. From Nas (1995).

To derive the governing nondimensional groups, it is customary to define a velocity:

$$U_T = \frac{\sigma_o R}{\alpha_o}. \tag{1}$$

The various nondimensional parameters can then be defined in terms of U_T: $Re = U_T R/\nu_o$, $Ma = U_T R/\alpha_o$, and $Ca = \mu U_T/\sigma_o$. We note that U_T is the rise velocity of a single spherical bubble in an unbounded fluid in the limit of zero Marangoni and Reynolds numbers. While most analytical and numerical work on thermocapillary motion has been confined to these limits, we do not make any such assumptions here.

The temperature is found by solving the energy equation

$$\frac{\partial \rho c_p T}{\partial t} + \nabla \cdot \rho c_p T \mathbf{u} = \nabla \cdot k \nabla T \tag{2}$$

where we have assumed that the fluid is incompressible and that viscous heating can be neglected. This equation is solved on a fixed grid by an explicit second order method in the same way as the momentum equation. The temperature at the surface of the bubble or drop is found by interpolating it from the grid and surface tension is found by

$$\sigma = \sigma_o - \beta(T - T_o). \tag{3}$$

Here, $\beta > 0$ since surface tension generally decreases with increasing temperature. In our studies, we have taken β to be a constant, though that is not necessary. The rest of the algorithm is identical to the method described in part I of these notes.

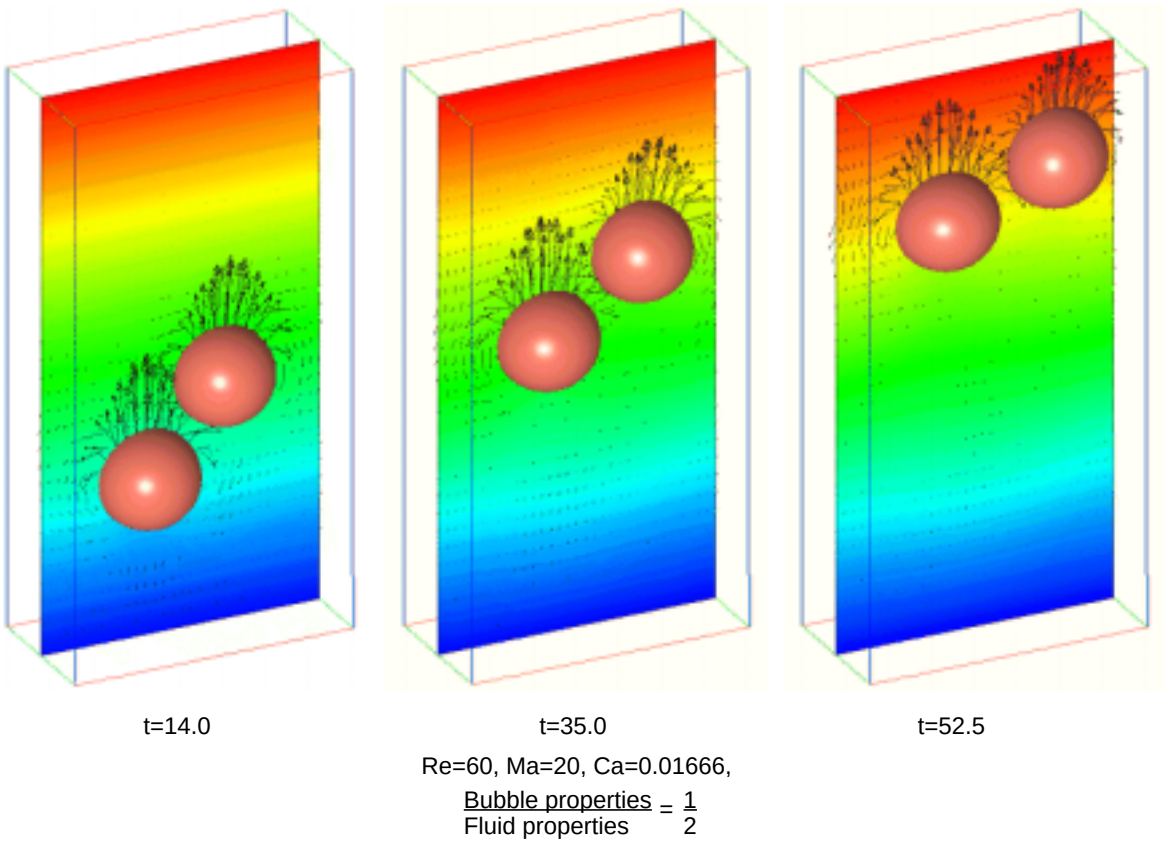

Figure 3: Thermocapillary migration of two three-dimensional bubbles. The bubbles and the isotherms are shown at three times. From Nas (1995).

Computations have shown that two equal size bubbles moving in a temperature field due to temperature dependent surface tension, interact strongly when the Marangoni and Reynolds numbers are finite. This contrasts results for zero values of these numbers which show that each bubble moves independently of the other bubbles. The interactions cause the bubbles to line up perpendicular to the temperature gradient and space themselves evenly across the channel. Figure 2 shows the bubble shape and the temperature field for two bubbles (all material properties of the bubble are 1/25 of the ambient fluid) at Re=Ma=40. Although each bubble starts at a different distance from the hot wall, they rise side-by-side most of the way. We have examined the two bubble problem for several other values of the governing parameters and generally find the same behavior. The reason is relatively obvious: as the bubbles rise, the bubble on the left first catches up with the bubble on the right. It draws hot fluid down its side and as the bubble on the right rises, some of this fluid is drawn into its wake, thereby reducing slightly the temperature increase across the bubble on the right and hence its velocity. After the bubbles move slightly closer together, the fluid in the narrow gap between the bubbles is pushed down more than in the wider gap, since the contribution of each bubble to the velocity field adds in this region. This is seen in the second frame of the velocity field. Hence, more hot fluid is drawn into the narrow gap between the bubbles than into the wide one. As a result, the bubbles attract each other. After they collide, they bounce back and the bubble on the left pushes the bubble on the right to the right. The same evolution is also seen in three-dimensions, although it is slower. Figure 3 shows three frames from a computation with Re=60, Ma=20, and ratio of all properties equal to 0.5. In three-dimensions, however, the drops do not, appear to form the same "structures," and fluid shear generally disrupts the formation of bubble layers.

3 Solidifying Drops

Solidification of small droplets of molten metal impinging a cold surface has been studied extensively over the past two decades. Manufacturing applications based on drop deposition include various spray forming processes, as well as net-shape forming processes. In general, the molten metal drops have a diameter of 20-100 μm. Spray forming processes, involving high impact velocities of 100 m/s and high deposition frequency with little control over individual drop placement, produce slabs of material which still must be formed. On the other hand, lower impact velocities on the order of 5 m/s and control of both the momentum and trajectory of each drop make it possible to build up complex parts. The result is a net-shape process requiring no finishing procedures because molten material is deposited precisely where it is needed. Such a process has been called both digital microfabrication by Gao and Sonin (1994) and ballistic particle manufacturing, by Kruth (1991). The objective of this process is to deposit drops that do not disintegrate to form 'finger-like' lamellae, but to build up layers of drops into coherent three-dimensional structures. Our modeling of drop impingement and solidification is motivated by the recent experimental and theoretical studies of micro-manufacturing by Orme (1993) and Gao and Sonin (1994). Both authors have demonstrated that three-dimensional structures can be made by the precise deposition of droplets of molten material.

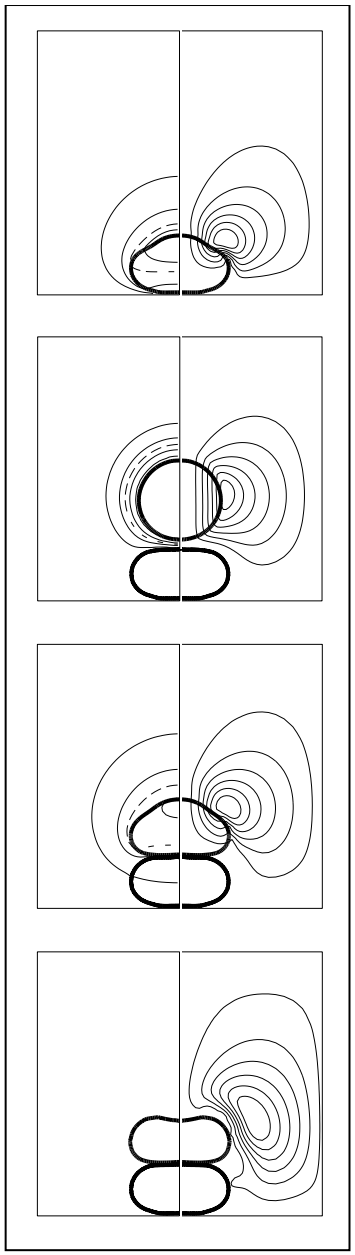

Figure 4: The collision and solidification of two hot drops with a cold wall. The drops are shown at four times. Isotherms are shown in the left half of the figure and streamlines in the right half. From Che, Ceccio, and Tryggvason (1998).

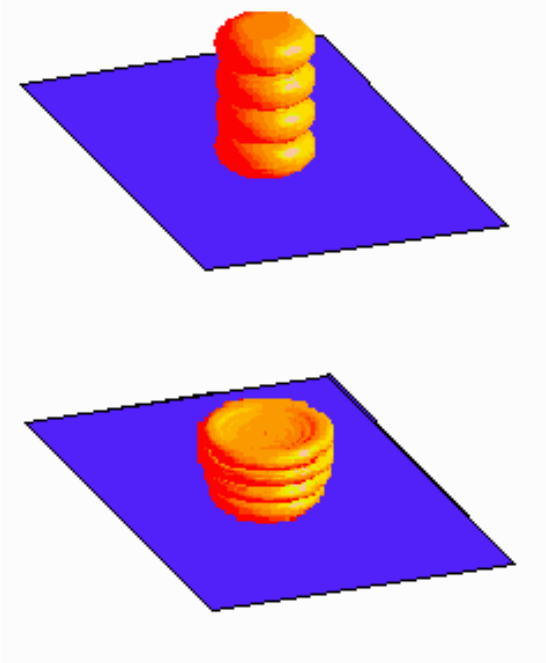

Figure 5: The final shape of four drops that collide with a cold wall and solidify. In the top frame, We and Pe are low, and the drops do not deform much. In the bottom frame We and Pe are high.

Drop deformation without solidification has been studied extensively beginning with the landmark work of Harlow and Shannon (1967), who used the "Marker And Cell" method to simulate the splash of a single liquid drop. Numerous computational models, which account for inertial, viscous, gravitational, and surface tension effects, have since been presented. Fukai *et al.* (1995) examined, for example, the effect of substrate wettability on drop spreading both experimentally and theoretically and found that the maximum splat radius decreases as the value of the advancing contact angle increases.

Several numerical models of drop deformation and solidification have been developed to simulate spray forming processes. Madjeski (1975) performed experiments and presented a simple theoretical model of spray forming which decoupled fluid flow and solidification. Recently, several authors, Bennett and Poulikakos (1994), Orme (1996), and Rangel and Bian (1996) have presented modified Madjeski models. Numerical models that fully couple fluid flow and solidification have also been presented. The numerical methods of Trapaga *et al.* (1992) using FLOW-3D and of Liu *et al.* (1993) using RIPPLE are similar in many ways. Both methods use a standard volume of fluid formulation to represent the gas-liquid interface and a continuum model for the solid-liquid interface in axi- symmetric coordinates. Trapaga *et al.* (1992) models surface tension forces with an equivalent surface pressure and solves for a single drop, while Liu *et al.* (1993) uses a continuum surface force (CSF) model and solves for cases of one drop and two drops. A much more complete analysis of a single solidifying drop has recently been presented by Waldvogel and Poulikakos (1997) who extend the Lagrangian finite element model of Fukai *et al.* (1995) to include a sharp solidification front. The results are compared with experiments

and used to explain the observed shape of the solidified drop.

We have focused on the solidification of multiple molten metal drops colliding with a cold wall, and the deposition of subsequent drops as the previously deposited material remelts and solidifies. The mathematical formulation accounts for inertial, viscous, gravitational, and surface tension effects for all phases and boundaries, but neglects thermal contact resistance, contact angle effects. Currently, the method does not allow drops to coalescence. The method presented in note I is used to explicitly track the position of the drop front. Heat transfer is characterized by conduction of heat through the solid and the outer fluid, and latent heat effects are neglected.

Figure 4 shows the deformation pattern for a low Weber number drop impingement and solidification with temperature contours given on the left and streamlines on the right. The temperature contour representing the freezing point is identified by a dashed line. Figure 4 shows the deposition of two drops with We = 2, Pe = 2.5. In the first two frames, the first drop impinges on the substrate and spreads radially outward until the drop front reaches full extension and solidifies. The last two frames show the impact and solidification of the second drop. The second drop requires more time to solidify due to the partial remelting of the first drop as they collide. With more time, the second drop reaches full extension and continues to flow. The fluid at the center of the drop flows outward and depletes as the outer edge thickens.

Figure 5 shows the final solidified shape of four drops deposited on top of each other. In the top figure, We=60 and Pe=6 and in the bottom figure We=2 and Pe=2.5. The shape of the stack of drops depends strongly on the governing parameters. A high Weber and Peclet number case results in large deformation and several drops deposited on top of each other will produce a short, squat tower. Low Weber and Peclet numbers will, on the other hand, result in tall, slender towers. More details can be found in Che, Ceccio, and Tryggvason (1998).

4 Solidification Without Flow

While the simple solidification model presented in the last section allows us to capture certain aspects of the interaction of flow with phase change, it is often necessary to use a more complete description of the phase change. Before we attempt to simulate problems in which it is necessary to account for both flow and phase change, we will first examine phase change without flow. In the simplest case of a pure material, the problem is reduced to solving one equation for the heat conduction in the material. Since a phase change takes place at T_m, there is a release of latent heat at the boundary, and this heat source must be included in the energy equation. For binary alloys, another material is dissolved in the main material, and it becomes necessary to account for mass diffusion along with conduction of heat.

A number of authors have examined the solidification of both pure materials as well as alloys in the absence of flow. We refer the reader to Juric and Tryggvason (1996) for a discussion of work on pure materials. For binary alloys, the studies have been partially motivated by interest in directional solidification. The translation velocity, the temperature gradient in the furnace, and the initial alloy composition are the controllable process

variables which determine the microstructure and the physical properties of the final solidified part. The liquid-solid interface during solidification is generally not planar but forms a cellular or dendritic structure depending on the processing conditions. Understanding and linking the behavior and geometry of the interface to the processing conditions is then of crucial importance to metallurgists. Mullins and Sekerka (1964) performed a linear stability analysis of the interface under more general conditions, but previously this understanding has been mostly empirical. More recently, researchers modeling directional solidification numerically have attempted to overcome the many simplifying assumptions of the previous analyses to provide more comprehensive quantitative predictions. Ungar and Brown (1985) have developed boundary conforming finite element methods to study the growth and stability of solidification cells in greater detail. Wheeler *et al.* (1992,1993), Boettinger *et al.* (1994), and Warren and Boettinger (1995) have developed phase-field models for isothermal solidification of a binary alloy. A comprehensive review of methods for alloy solidification and morphological stability theory is provided by Coriell and McFadden (1993).

Here, we describe a front-tracking method to solve the directional solidification problem. The fully coupled solute and energy equations for a dilute binary alloy are solved, and the effects of latent heat, unequal material properties between liquid and solid and unsteady effects are completely taken into account.

4.1 Formulation

For the problem of solidification of a dilute binary alloy, we write the governing solute and energy equations for both the liquid and solid phases simultaneously. The densities of the liquid and solid phases are assumed to be equal and constant. Volume contraction and expansion, as well as fluid convection effects are thereby neglected. The thermal conductivity, volumetric specific heat, and chemical diffusivity of each phase are assumed to be constant but not necessarily equal.

The energy equation is written as:

$$\frac{\partial}{\partial t}\left(cT\right) = \nabla \cdot K \nabla T + Q \tag{4}$$

where c is the volumetric specific heat, K is the thermal conductivity and

$$Q = \int_{\mathcal{A}} q\delta\left(\mathbf{x} - \mathbf{x}_f\right) d\mathcal{A} \; . \tag{5}$$

$\delta\left(\mathbf{x} - \mathbf{x}_f\right)$ is a three-dimensional delta function that is non-zero only at the interface where $\mathbf{x} = \mathbf{x}_f$. q is the energy source due to liberation or absorption of the volumetric latent heat, L, at the interface

$$q = L\mathbf{V} \cdot \mathbf{n} \; . \tag{6}$$

$\mathbf{V} = \left(d\mathbf{x}_f/dt\right)$ is the interface velocity and $\mathbf{n}$ is the normal to the interface. In this equation, L takes into account unequal specific heats

$$L = L_o + \left(c_1 - c_2\right) T_m \; . \tag{7}$$

L_o is the customary latent heat measured at the reference equilibrium melting temperature of the pure material, T_m. The subscript 1 refers to the solid phase and 2 to the liquid phase.

The solute equation is written for both phases separately as:

$$\frac{\partial C_1}{\partial t} = \nabla \cdot D_1 \nabla C_1 \quad \text{and} \quad \frac{\partial \mathrm{C}_2}{\partial \mathrm{t}} = \nabla \cdot \mathrm{D}_2 \nabla \mathrm{C}_2 \tag{8}$$

where C is the solute concentration. The solute balance at the interface then requires that

$$(D_2 \nabla C_2 - D_1 \nabla C_1) \cdot \mathbf{n} = C_2(k-1)\mathbf{V} \cdot \mathbf{n} \tag{9}$$

where $k = C_1(\mathbf{x}_f(t))/C_2(\mathbf{x}_f(t))$ is the partition coefficient and is assumed to be constant.

To recast Eqs.(8) and (9) in the form of a single equation for both phases, we define new variables for the solute concentration and diffusivity as:

$$(\tilde{C}, \tilde{D}) = \begin{cases} (C_1/k, kD_1), & \text{in the solid,} \\ (C_2, D_2), & \text{in the liquid} \end{cases} \tag{10}$$

Then the single field representation is:

$$\frac{\partial \tilde{C}}{\partial t} = \nabla \cdot \tilde{D} \nabla \tilde{C} + S \ . \tag{11}$$

S is the source term which accounts for rejection or absorption of the solute at the interface

$$S = \int_{\mathcal{A}} s\delta \left(\mathbf{x} - \mathbf{x}_f\right) d\mathcal{A} \ . \tag{12}$$

and s is the source of solute

$$s = \tilde{C}_f \left(1 - k\right) \mathbf{V} \cdot \mathbf{n} \tag{13}$$

where $\tilde{C}_f = \tilde{C}(\mathbf{x}_f(t))$ is the value of the transformed concentration at the interface. Note that the transformed concentration is continuous at the interface. Since the interface is tracked, we can regain the original concentration and diffusivity fields from the known position of the interface by:

$$C = \tilde{C} + \left(k\tilde{C} - \tilde{C}\right) I(\mathbf{x}) \ . \tag{14}$$

$I(\mathbf{x})$ is a material indicator function similar to the density in note I. It is 1 in phase 1 and 0 in phase 2. This function also allows us to evaluate the values of the thermal conductivity and specific heat at every location by

$$K(\mathbf{x}) = K_2 + (K_1 - K_2)\, I(\mathbf{x}) \tag{15}$$

and similarly for the specific heat.

In addition to the governing equations, an interface condition on the temperature must be satisfied at the phase boundary. This condition, taken from Alexiades and Solomon (1993), is given as:

$$T_f - T_m + \frac{T_m \left(c_2 - c_1\right)}{L_o} \left[T_f \ln \frac{T_f}{T_m} + T_m - T_f\right]$$

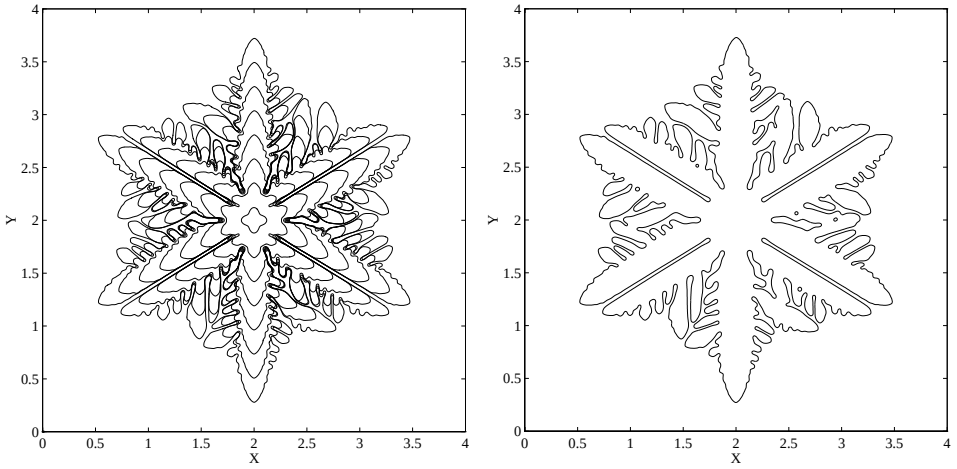

Figure 6: Growth of seed of pure material into an undercooled liquid. In (a), the interface is not allowed to coalesce, but in (b) the dendritic arms have fused together. From Juric and Tryggvason (1996).

$$+\frac{\sigma(\mathbf{n})T_m}{L_o}\kappa - m\tilde{C}_f + \frac{\mathbf{V}\cdot\mathbf{n}}{\nu(\mathbf{n})} = 0 \tag{16}$$

where $T_f = T(\mathbf{x}_f(t))$ is the interface temperature, $\sigma(\mathbf{n})$ and $\nu(\mathbf{n})$ are the anisotropic surface tension and kinetic mobility respectively. κ is twice the mean curvature which is positive when the center of curvature lies in the solid phase and m is the slope of the liquidus line which is assumed to be a constant.

The numerical construction of the indicator function from the tracked interface and other details of the numerical method are essentially the same as described in part I of these notes. The binary alloy problem requires only minor, straightforward modifications to that method: Equations (4) and (11), are discretized using a conservative, second order, centered difference scheme for the spatial variables. We use an explicit, first order, forward Euler time integration method for short time calculations and a second order time integration method for calculations that require accuracy over a longer time. The interface is represented by separate, non-stationary computational points connected to form a one-dimensional front which lies on the two-dimensional stationary mesh. The front is used to advect the discontinuous material property fields and to calculate interface curvature and normal velocity. Information is passed between the moving interface and the stationary grid as described in part I of these notes.

4.2 Results

We start by showing an example of the solidification of a pure material. Figure 6(a), shows the growth of a dendrite when a small seed grows in an undercooled melt. We solve the problem on the full domain and do not impose any symmetry requirement on the interface shape. The primary physical parameters are the dimensionless undercooling, St, the capillary parameter, σ, and the ratio of heat capacities and thermal conductivites in the solid and liquid regions. The process of solidification in an undercooled liquid is

inherently unstable and sensitive to initial conditions. The degree of instability in the growing solid depends on the choice of physical parameters. Typically, for high σ and low St the liquid-solid interface remains smooth for a long time while for low σ and high St the interface deforms quickly into branching dendrites. In Figure 6(a), the value of σ is relatively low requiring an 800×800 grid to capture the smallest scales accurately. In Figure 6(a), we did not allow dendritic arms to fuse together. When coalescence is allowed, by simply merging interfaces that are close together, the small scale structure changes slightly, but the overall structure remains the same. Figure 6(b) shows the interface shape for a simulation with coalescence at the same time as the interface in Figure 6(a).

Figure 7 shows a single frame from a simulation of the directional solidification of a binary alloy. The computation is performed in a two-dimensional rectangular domain which is periodic in the x-direction. Initially the upper portion of the domain is liquid and is separated from the solid in the lower portion by the solid-liquid interface, which is initially nearly planar with a small amplitude cosine perturbation. The governing parameters are selected such that the interface is unstable and the solute rejected at the solidification front accumulates between the advancing cells. The lighter shades of gray represent higher solute concentration and the white line is the interface. The rejection of solute ahead of the advancing interface and into the intercellular grooves is clearly visible. The grooves solidify eventually, freezing in the uneven solute concentration in the solid.

For other examples, including comparison with linear theory and other validation tests, see Juric and Tryggvason (1996) for the solidification of pure materials and Juric (1996) for binary alloys.

5 Boiling Flows

In many problems it is necessary to account for fluid flow governed by the Navier-Stokes in addition to transfer of energy and phase changes. Here, we present a method designed to handle such situations. Although the method has applications to a large range of problems, we have initially applied it to boiling. In film boiling from an upward facing, flat surface a layer of vapor completely blankets the heated surface. The vapor is constantly depleted by break off and rise of vapor bubbles and is replenished by vaporization of liquid at the liquid-vapor interface. The vapor layer acts as an insulator thereby lowering the heat transfer rate and increasing the heater surface temperature.

Efforts to understand the processes involved in boiling have focused mainly on simple numerical and analytical models of vapor bubble dynamics (Rayleigh, 1917 and Patil and Prusa, 1991). While a number of authors have modeled the growth of vapor bubbles in boiling, almost all use a number of simplifications. Examples of relatively recent such computation are Lee and Nydahl (1989) and Patil and Prusa (1991) who assume that the bubble has a hemispheric shape as it grows. Welch (1995) allows fully deformable, two-dimensional bubbles by using moving triangular grids but is only able to follow the evolution for a relatively short time. Son and Dhir (1997) use a moving body fitted coordinate system to simulate film boiling for both two-dimensional and axisymmetric flows, but can only follow the evolution up to the point of departure. Recently, the same authors have been experimenting with the use of level-set methods for phase changes.

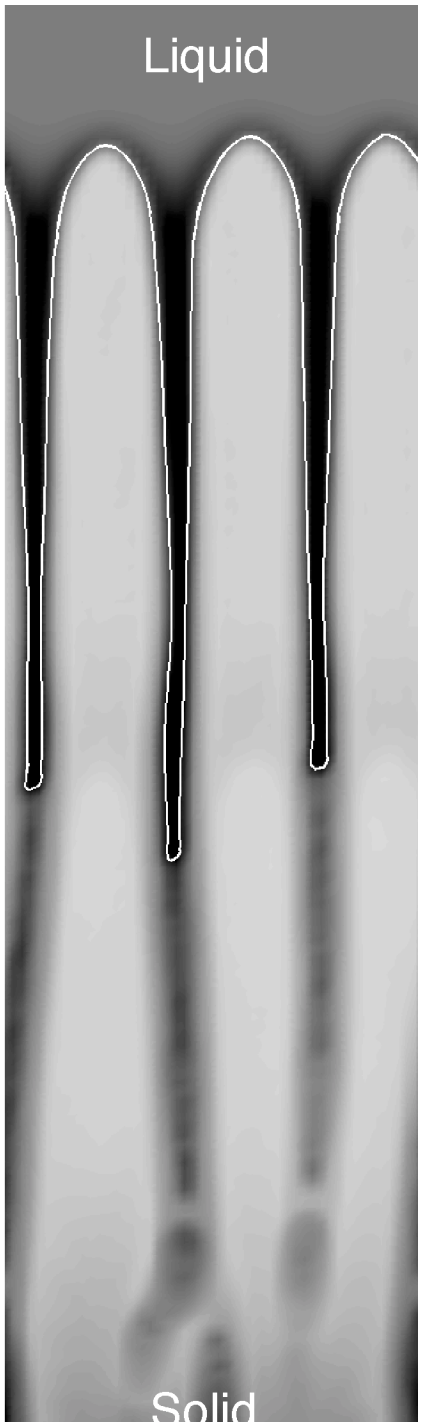

Figure 7: For an unstable case the interface deforms quickly, bifurcates and begins to grow in a cellular pattern. The lighter shades of gray represent higher solute concentration and the white line is the interface. The rejection of solute ahead of the advancing interface and into the intercellular grooves is clearly visible.

These methods allow more general interface deformation, but they report less accuracy than with the body fitted mesh, at least so far.

5.1 Formulation

As before we write the governing equations for both phases simultaneously. However we must now also take into account mass transfer across the interface and force as well as energy sources at the interface. Note that in two-phase flow, additional terms appear in these equations due to the phase change and the fact that the interface is no longer a material interface. The fluid velocity at the interface and the interface velocity are unequal. This single field, local instant formulation incorporates the interface jump conditions into the governing equations as sources which act only at the interface. Kataoka (1985) shows that this single field representation is equivalent to the local instant formulations of Ishii (1975) and Delhaye (1974). They formulate the phase change problem in terms of local instant variables for each phase with appropriate jump conditions at the moving phase interface. These local instant formulations form the basis for formulations using various types of averaging.

The momentum equation is written for the entire flow field and the forces due to surface tension are inserted at the interface as body forces which act only at the interface. In conservative form this equation is

$$\frac{\partial}{\partial t}(\rho \mathbf{u}) + \nabla \cdot (\rho \mathbf{u}\mathbf{u}) = -\nabla P - \rho \mathbf{g} + \nabla \cdot \mu\Big(\nabla \mathbf{u} + \nabla \mathbf{u}^T\Big) + \mathbf{F} \ . \tag{17}$$

The notation follows customary convention: $\mathbf{u}$ is the fluid velocity field, P is the pressure, ρ is the density and μ is the viscosity. $\mathbf{F}$ is a source term which accounts for forces acting on the interface

$$\mathbf{F} = \int_{\mathcal{A}} \mathbf{f} \delta \left(\mathbf{x} - \mathbf{x}_f\right) d\mathcal{A} \ . \tag{18}$$

$\mathbf{f}$ is the surface tension normal to the interface,

$$\mathbf{f} = \sigma \kappa \mathbf{n} \tag{19}$$

The conservation of mass equation for a fluid with a volume expansion at the interface due to phase change is

$$\nabla \cdot \rho \mathbf{u} = M \tag{20}$$

where

$$M = \int_{\mathcal{A}} m \delta \left(\mathbf{x} - \mathbf{x}_f\right) d\mathcal{A} \tag{21}$$

and m accounts for the change in density due to the motion of the phase boundary

$$m = (\rho_1 - \rho_2)\, \mathbf{V} \cdot \mathbf{n} \ . \tag{22}$$

Note that this formulation of Eq.(20) is equivalent to the customary statement of the conservation of mass principle. The subscript 1 will refer to the vapor phase and 2 to the liquid phase.

The energy equation is

$$\frac{\partial}{\partial t}\left(\rho c T\right) + \nabla \cdot \left(\rho \mathbf{u} c T\right) = \nabla \cdot K \nabla T + Q \tag{23}$$

where

$$Q = \int_{\mathcal{A}} q \delta \left(\mathbf{x} - \mathbf{x}_f\right) d\mathcal{A} \ . \tag{24}$$

q is the energy source due to liberation or absorption of latent heat, L, at the interface

$$q = \rho_1 L \left(\mathbf{V} - \mathbf{u}_1\right) \mathbf{cdotn} \ . \tag{25}$$

$\mathbf{u}_1$ is the vapor phase fluid velocity at the interface. In this equation L takes into account unequal specific heats:

$$L = L_o + \left(c_2 - c_1\right) T_v \ . \tag{26}$$

L_o is the customary latent heat measured at the reference equilibrium vaporization temperature, T_v .

The interface temperature condition that must be satisfied on the phase boundary [2] is

$$\begin{aligned} T_f - T_v - \frac{\sigma T_v \kappa}{2 L_o}\left(\frac{1}{\rho_2} + \frac{1}{\rho_1}\right) + \frac{T_v}{L_o}\left(\frac{1}{\rho_2} - \frac{1}{\rho_1}\right)\left(P_f - P_\infty\right) \\ - \left(c_2 - c_1\right)\frac{T_v}{L_o}\left[T_f \ln \frac{T_f}{T_v} + T_v - T_f\right] = 0 \ , \end{aligned} \tag{27}$$

where P_∞ and P_f are the ambient pressure and the pressure at the interface in the vapor respectively. To complete the formulation we specify the material property fields using the material indicator function, $I(\mathbf{x})$, as discussed in the previous section.

It is important to note that integration of Eqs.(17), (20) and (23) across the interface directly yields the correct jump conditions in the local instant formulation for two-phase systems given by Delhaye (1974) and Ishii (1975) with the assumptions that the interface is thin and massless and that the bulk fluids are incompressible. However, we allow for volume expansion at the interface in the conservation of mass, Eq.(20), but neglect the volume expansion term in the constitutive shear relation in the momentum, Eq.(17). In the energy equation, viscous dissipation and kinetic energy contributions from the product of the fluid velocity at the interface and the interface velocity are neglected. Contributions to the energy equation from interface stretching are usually small compared with the latent heat and are neglected. Thermocapillary effects are also neglected.

The details of the finite difference/front-tracking method used to solve the above system of equations will not be discussed here but are provided in Juric and Tryggvason (1998).

5.2 Results

Figure 8 shows four frames from a simulation of film boiling of hydrogen at 8 atm pressure where we follow the evolution of an unstable vapor layer below a liquid layer which is below another vapor layer. The domain is periodic in the x-direction and to allow for

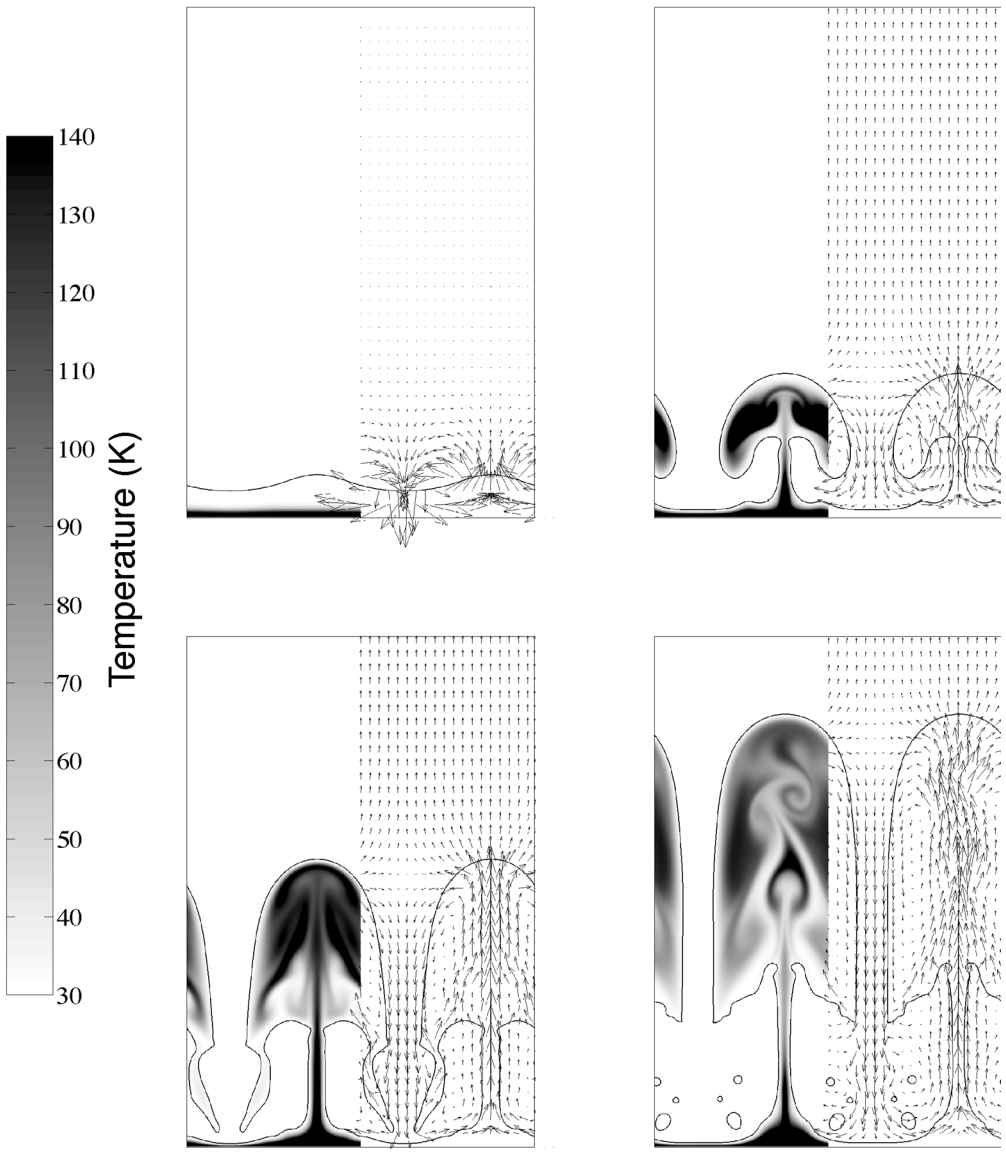

Figure 8: Film boiling simulation at four different times. The bubble surface, the temperature field, and the velocity is shown.

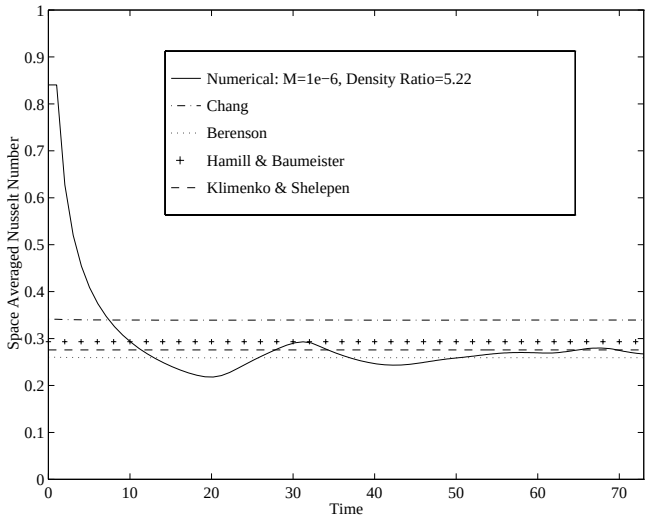

Figure 9: Comparison of heat transfer results from a two-dimensional simulation with several experimental correlations (Klimenko, 1981).

vaporization we let fluid exit at the top boundary where we specify the ambient pressure to be zero. The temperature field is initially zero everywhere with a heat flux, q_w, applied to the rigid bottom wall. The domain size is $1.33 \times 4mm$ and the grid resolution is 300×600 grid points. The wall heat flux is $44W/cm^2$ and the Reynolds number based on bubble tip velocity is 525. The density ratio is 5.22, the viscosity ratio is 3.37, thermal conductivity ratio is 3.42, specific heat ratio is 0.88, and the Prandtl number of liquid is 1.51. The solid black lines are the liquid-vapor interfaces and the arrows represent velocity vectors. The temperatures are shown as shades of gray where the hottest regions are near the bottom wall and the coolest regions are in the liquid which remains nearly isothermal. The velocity vectors show that vapor generated near the wall is jetted into the rising bubble while cold liquid falls toward the wall between the bubbles.

Nusselt number is not set beforehand but is determined by the calculation of the wall temperature, T_w. In Figure 9, the heat transfer results ¿from two-dimensional numerical simulations is compared against experimental correlation by Klimenko (1981). The heat transfer rate changes with time, but with the exception of the initial transient, the results are surprisingly good although our two-dimensional numerical results are consistently lower than the values ¿from three-dimensional experiments. However we would expect our two-dimensional results to exhibit lower heat transfer for several reasons. In three dimensions the heat flow is not confined to a plane. There are also more bubbles rising from many various points on a heated surface. On average the height of the vapor layer above the heated wall would be lower and thus the heat transfer would be higher in three-dimension than in two-dimension.

6 Conclusions

We have shown in this note that the method described in note I can be extended to deal with heat transfer, variable surface tension, and phase change. Nearly all materials used by man are at some point processed in their fluid state. The phase transition to solid is usually the determining factor in the ultimate properties of the final product. Residual stresses in polymeric products, voids in turbine blades, are only a few examples of defects that cause major problems. The ability to simulate the solidification process directly holds the promise to revolutionize the mathematical modeling and hence our understanding of these processes. The ability to do useful simulations of the formation of microstructures, for example, requires appropriate algorithms and computers that are large and fast enough. While considerable algorithm development is still needed, the examples shown here suggest that we can expect a high degree of success within the next few years. Consider the formation of microstructures in solidifying materials. It is not unreasonable to expect that we would have to resolve length scales from $O(10\mu m)$ to $O(1mm)$ in order to gain useful information about the final properties of the material. If we assume that about 10 grid points are needed for the smallest scales, we need grids of $O(1000^3)$. This should be possible within a few years.

References

[1] A. Acrivos, D. J. Jeffrey and D. A. Sauille, "Particle Migration in Suspension by Thermocapillary or Electrophoretic Motion," *J. Fluid Mech.***212**, p. 95-110 (1990).

[2] V. Alexiades and A. D. Solomon, *Mathematical Modeling of Melting and Freezing Processes,* Hemisphere, Washington, DC, p. 92, (1993).

[3] T. Bennett and D. Poulikakos, "Heat Transfer Aspects of Splat-Quench Solidification: Modelling and Experiment," *J. Material Science* **29** , p. 2025-2039, (1994).

[4] W. J. Boettinger, A. A. Wheeler, B. T. Murray and G. B. McFadden, "Prediction of Solute Trapping at High Solidification Rates Using a Diffuse Interface Phase-Field Theory of Alloy Solidification," *Mat. Sci. Eng. A* **178**, p. 217-223, (1994).

[5] W. N. Bond, "Bubbles and Drops and Stokes' law," *Phil. Mag.* **4**(24), p. 889, (1927).

[6] W. N. Bond and D. A. Newton, "Bubbles, Drops, and Stokes' law (paper 2)," *Phil. Mag.* **5**(31), p. 794, (1928).

[7] K. Brattkus and D. I. Meiron, "Numerical Simulations of Unsteady Crystal Growth," *SIAM J. Appl.Math.* **52**, p. 1303-1320, (1992).

[8] R. J. Braun, G. B. McFadden and S. R. Coriell, "Morphological Instability in Phase-Field Models of Solidification," *Phys. Rev. E* **49**, p. 4336-4352, (1994).

[9] J. Che, S.L. Ceccio and G. Tryggvason, "Computations of the Deformation and Solidification of Impinging Molten Metal Drops," submitted to *J. Fluid Engineering,* (1998).

[10] S. R. Coriell and G. B. McFadden, "Morphological Stability," in *Handbook of Crystal Growth, Vol. 1,* edited by D. T. J. Hurle, North-Holland, Amsterdam, p.785-857, (1993).

[11] J.M. Delhaye, "Jump Conditions and Entropy Sources in Two-Phase Systems. Local Instant Formulation," *Int. J. Multiphase Flow* **1**, p. 395-409, (1974).

[12] A. Frumkin and V. G. Levich, *Zh. Fiz. Khim.* **21**, p. 1183, (1947).

[13] J. Fukai, Y. Shiiba, T. Yamamoto, O. Miyatake, D. Poulikakos, C. M. Megaridis and Z. Zhao, "Wetting Effects on the Spreading of a Liquid Droplet Colliding with a Flat Surface: Experiment and Modeling," *Phys. Fluids* **7**(2), p. 236-247, (1995).

[14] F. Gao and A. Sonin, "Precise Deposition of Molten Microdrops: The Physics of Digital Microfabrication," *Proc. R. Soc. Lond. A* **444**,

[15] J. Hadamard, "Mouvement Permanent Lent d'une Sphère Liquide et Visqueuse dans une Liquide Visqueux," *C. R.. Acad. Sci.* **152**, p. 1735, (1911).

[16] W. L. Harberman and R. K. Morton, "An Experimental Study of Bubbles Moving in Liquids," *Trans. ASCE* **121**, p. 227, (1956).

[17] F. H. Harlow and J. P. Shannon, "The Splash of a Liquid Drop," *J. Appl. Physics***38**, p. 3855, (1967).

[18] J. F. Harper, "The Motion of Bubbles and Drops through Liquids," *Adv. Appl. Mech.* **12**, p. 59, (1972).

[19] J. F. Harper, "On Bubbles with Small Immobile Adsorbed Films Rising in Liquids at Low Reynolds Numbers," *J. Fluid Mech.* **58**, p. 539, (1973).

[20] M. Ishii, *Thermo-Fluid Dynamic Theory of Two-Phase Flow,* Eyrolles, Paris, (1975).

[21] D. Juric and G. Tryggvason, "A Front Tracking Method for Dentritic Solidification," *J. Comput. Phys.* **123**, p. 127-148, (1996).

[22] D. Juric and G. Tryggvason, "Directional Solidification of Binary Alloys using a Front-Tracking Method," in preparation.

[23] D. Juric and G. Tryggvason. "Computations of Boiling Flows," accepted by *Int'l. J. Multiphase Flow.*

[24] I. Kataoka, "Local Instant Formulation of Two-Phase Flow", Technical Report Institute of Atomic Energy, Kyoto University, Kyoto, Japan, Vol. 203, p. 1-33, (1985).

[25] V. V. Klimenko, "Film Boiling on a Horizontal Plate - New Correlation," *Int. J. Heat and Mass Transfer* **24**, p. 69-79, (1981).

[26] R. Kobayashi, "Simulations of Three-Dimensional Dendrites," in Pattern Formation in Complex Dissipative Systems, Edited by S. Kai, World Scientific, Singapore, p. 121-128, (1992).

[27] J. P. Kruth, "Material Incress Manufacturing by Rapid Prototyping Techniques," *Annals of the CIRP* **40**/2, p. 603-614, (1991).

[28] R. C. Lee and J. E. Nydahl, "Numerical Calculations of Bubble Growth in Nucleate Boiling from Inception through Departure," *J. Heat Transfer* **111**, p. 474-479, (1989).

[29] H. Liu, E. J. Lavernia and R. H. Rangel, "Numerical Simulation of Substrate Impact and Freezing of Droplets in Plasma Spray Processes," *J. Appl. Phys.* **26**, p. 1900-1908, (1993).

[30] A. Liu, J. E. Voth and T. L. Bergman, "Pure Material Melting and Solidification with Liquid Phase Bouyancy and Surface Tension Force," *Int. J. Heat Mass Transfer* **36**, p. 411-422, (1993).

[31] J. Madjeski, "Solidification of Droplets on a Cold Surface," *Int. J. Heat Mass Transfer* **19**, p. 1009-1013, (1975).

[32] W. W. Mullins and R. F. Sekerka, "Stability of a Planar Interface During Solidification of a Dilute Binary Alloy," *J. Appl. Phys.,* **35**, p. 444-451, (1964).

[33] S. Nas, "Computational Investigation of Thermocapillary Migration of Bubbles and Drops in Zero Gravity," *Ph.D. Thesis,* The University of Michigan, (1995).

[34] S. Nas and G. Tryggvason, "Computational Investigation of the Thermal Migration of Bubbles and Drops," in AMD 174/FED 175 Fluid Mechanics Phenomena in Microgravity, Ed. Siginer, Thompson and Trefethen. p. 71-83, Presented at the ASME 1993 Winter Annual Meeting, ASME (1993).

[35] M. Orme, "A Novel Technique of Rapid Solidification Net-For Materials Synthesis," *J. Materials Engineering and Performance* /bf2(3), p. 399-405, (1993).

[36] M. E. Orme, C. Huang, and J. Courter, "Precision Droplet-based Manufacturing and Material Synthesis: Fluid Dynamics and Thermal Control Issues," *Atomization and Sprays* /bf6, p. 305-329, (1996).

[37] R. K. Patil and J. Prusa, "Numerical Solutions for Asymptotic, Diffusion Controlled Growth of a Hemispherical Bubble on an Isothermally Heated Surface," in *Experimental/Numerical Heat Transfer in Combustion and Phase Change,* edited by M. F. Modest, T. W. Simon and M. Ali Ebadian, HTD-Vol. 170, ASME, New York, (1991).

[38] R. H. Rangel and X. Bian, "Metal-Droplet Deposition Model Including Liquid Deformation and Substrate Remelting", *Int. J. Heat Mass Transfer* ¿**40**(11), p. 2549-2564, (1997).

[39] Lord Rayleigh, "On the Pressure Developed in a Liquid During the Collapse of a Spherical Cavity," *Phil. Mag.* **34**, p. 94-98, (1917).

[40] W. Rybczynski, "On the Translatory Motion of a Fluid Sphere in a Viscous Medium," *Bull. Int. Acad. Pol. Sci. Lett. Cl. Sci. Math. Natur.* **40**, (1911).

[41] A. Schmidt, "Computations of Three Dimensional Dendrites with Finite Elements," *J. Comp. Phys.* **126**, (1996).

[42] P. R. Schunk and R. R. Rao, "Finite Element Analysis of Multicomponent Two-phase Flows with Interphase Mass and Momentum Transport," *Int. J. Num. Meth. Fluids* **18**, p. 821-842, (1994).

[43] W. Shyy and M. M. Rao, "Enthalpy Based Formulations for Phase-Change Problems with Applicaiton to G-Jitter," *Microgravity Science and Technology* **7**:1, p. 41-49, (1994).

[44] G. Son and V. K. Dhir, "Numerical Simulation of Saturated Film Boiling on a Horizontal Surface," *J. Heat Mass Trans - Trans. ASME* **119**(3), p. 525-533, (1997).

[45] C. R. Swaminathan and V. R. Voller, "On the Enthalpy Method," *Int. J. Num. Meth. Heat Fluid Flow* **3**, p. 233-244, (1993)

[46] G. Trapaga, E. F. Matthys, J. J. Valencia and J. Szekely, "Fluid Flow, Heat Transfer, and Solidification of Molten Metal Droplets Impinging on Substrates: Comparison of Numerical and Experimental Results," *Metall. Trans. B* **23**B, p. 701-718, (1992).

[47] L. H. Ungar and R. A. Brown, "Cellular Interface Morphologies in Directional Solidification IV. The Formation of Deep Cells," *Phys. Rev. B* **31**, p. 5931-5940, (1985).

[48] J. M. Waldvogel and D. Poulikakos, Solidification phenomena in picoliter size solder droplet deposition on a composite substrate," *Int. J. Heat Mass Transfer* **40**(2), p. 295-309, (1996).

[49] J. A. Warren and W. J. Boettinger, "Prediction of Dendritic Growth and Microsegregation Patterns in a Binary Alloy Using the Phase-Field Method," *Acta Metall.* **43**, p. 689-703, (1995).

[50] S. W. J. Welch, "Local Simulation of Two-Phase Flows Including Interface Tracking with Mass Transfer," *J. Comp. Phys.* **121,** p. 142-154, (1995).

[51] A. A. Wheeler, W. J. Boettinger and G. B. McFadden, "Phase-Field Model for Isothermal Phase Transitions in Binary Alloys," *Phys. Rev. A* **45**, p. 7424-7439, (1992).

[52] A. A. Wheeler, B. T. Murray and R. J. Schaefer, "Compuations of Dendrites Using a Phase-Field Model," *Physica D* **66**, p. 243-262, (1993).